remote sensing

MDPI

Article

Multi-Scale Assessment of Nighttime Heat Health Risk and Dominant Factors Using MODIS and SDGSAT-1 Observations

Zhuang Tan [1], Qixia Man [1,*], Baolei Zhang [1], Pinliang Dong [2], Haiying Sun [3], Zhongchang Sun [4,5,6], Linlin Lu [4,5,6], Changyong Dou [4,5,6], Xinming Yang [7], Changyin Han [1], Cong Zhou [1], Xiaoqi Sun [1], Jian Wang [1] and Zizhen Li [1]

[1] College of Geography and Environment, Shandong Normal University, Jinan 250014, China; 2024215071@stu.sdnu.edu.cn (Z.T.); blzhangsd01@sdnu.edu.cn (B.Z.); 2023026804@stu.sdnu.edu.cn (C.H.); 2024215060@stu.sdnu.edu.cn (C.Z.); 2025215063@stu.sdnu.edu.cn (X.S.); 2025215075@stu.sdnu.edu.cn (J.W.); 2025215080@stu.sdnu.edu.cn (Z.L.)
[2] Department of Geography and the Environment, University of North Texas, Denton, TX 76203, USA; pinliang.dong@unt.edu
[3] Jinan Rail Transit Group Construction Investment Co., Ltd., Jinan 250100, China; jinanguidaojt@163.com
[4] International Research Center of Big Data for Sustainable Development Goals, Beijing 100094, China; sunzc@aircas.ac.cn (Z.S.); lull@radi.ac.cn (L.L.); doucy@aircas.ac.cn (C.D.)
[5] Aerospace Information Research Institute, Chinese Academy of Sciences, Beijing 100094, China
[6] University of Chinese Academy of Sciences, Beijing 100049, China
[7] Jinan Environmental Research Institute, Jinan 250098, China; yangxinming@jnep.cn
* Correspondence: qixiaman@sdnu.edu.cn

Highlights

What are the main findings?

- A multi-scale framework links MODIS-based provincial screening with SDGSAT-1-based block-level assessment of nighttime heat health risk.
- Higher-risk units generally involve more complex dominant factor configurations, and LCZ types are associated with distinct dominant-factor patterns.

What are the implications of the main findings?

- The framework supports differentiated adaptation across spatial scales by identifying where nighttime heat health risk is concentrated and which risk components dominate.
- High-resolution SDGSAT-1 nighttime observations improve fine-scale identification of intra-urban heat health risk and its dominant factors.

Abstract

Climate change is amplifying heat-related health risks, making heat health risk assessment increasingly important for sustainable urban development. However, current studies still face three challenges: (1) macro-scale and fine-scale assessments remain weakly linked; (2) nighttime heat health risk has received limited attention; and (3) dominant factor identification remains insufficient, especially within the Local Climate Zone (LCZ) framework. To address these gaps, this study developed a hazard–exposure–vulnerability-based, multi-scale framework for assessing nighttime heat health risk in Shandong Province, China. At the macro scale, MODIS nighttime land surface temperature (1 km) was used to characterize heat hazard, and district-level risk was assessed by integrating socio-statistical data. Hotspot analysis was then applied to identify high-risk clusters and select cities for fine-scale assessment. At the fine scale, SDGSAT-1 thermal infrared data (30 m) were used to characterize intra-urban nighttime heat hazard, and block-level risk was assessed by integrating socioeconomic and urban infrastructure data. Dominant risk factors were further identified for each spatial unit. Results show that (1) at the macro scale, high nighttime heat

Check for updates

Academic Editor: Janet Nichol

Received: 22 May 2026
Revised: 23 June 2026
Accepted: 4 July 2026
Published: 7 July 2026

Copyright: © 2026 by the authors. Licensee MDPI, Basel, Switzerland. This article is an open access article distributed under the terms and conditions of the Creative Commons Attribution (CC BY) license.

health risk districts are concentrated mainly in southern Shandong and major urban cores; (2) at the fine scale, overall risk is higher in inland cities than in the coastal city, and the inland cities show similar spatial patterns; (3) at both district and block units, higher risk levels are associated with more complex dominant factor configurations; and (4) compact high- and mid-rise zones (LCZ 1–2) are mainly characterized by multiple dominant factors, whereas open low-rise/sparsely built zones (LCZ 6/9) are mainly characterized by no dominant factor. This study provides a multi-level perspective for heat-risk governance, offers a scientific basis for both macro-scale policy formulation and fine-scale intervention, and contributes to more sustainable and resilient cities.

Keywords: urban heat; heat health risk assessment; dominant factors; local climate zones; SDGSAT-1

1. Introduction

Extreme heat has emerged as one of the most severe climate-related threats to urban societies under ongoing global warming [1,2]. According to the Sixth Assessment Report of the Intergovernmental Panel on Climate Change, global mean temperature has already increased by approximately 1.1 °C relative to the pre-industrial level. Under current emission trajectories, warming could reach about 3.2 °C by 2100. High temperatures can disturb thermal comfort and impair normal physiological regulation [3]. Sustained thermal stress can then interfere with body temperature control, thereby increasing the likelihood of heat exhaustion and heatstroke [4–6]. It can also impose additional strain on the cardiovascular system, with dehydration and circulatory stress further aggravating cardiovascular dysfunction [7]. When such thermal stress persists, these adverse effects may accumulate, eventually resulting in hospitalization or premature death [8]. Several of the most severe heat extremes since the beginning of the 21st century have collectively resulted in more than 260,000 deaths globally [9].

Beyond daytime heat, cities are experiencing increasingly elevated nighttime temperatures, along with more frequent and longer-lasting nocturnal heat events [10,11]. Nighttime heat poses a substantial health threat [12–14]. Under extreme hot-night conditions, mortality risk has been found to increase by approximately 30–50% compared with non-hot nights [15]. A separate global study of more than 14 million deaths further attributed approximately 84,000 deaths to nighttime heat [16]. Therefore, nighttime heat warrants greater attention [17], and assessing nighttime heat health risk is essential for climate adaptation and human-centered sustainable urban development.

Heat health risk assessment has increasingly been developed within a risk-oriented framework. Earlier IPCC studies mainly emphasized vulnerability to climate change, whereas later assessment frameworks defined risk as the interaction of hazard, exposure, and vulnerability [18]. This structure provides a systematic basis for evaluating heat-related health risks, and it has been widely adopted in recent climate-risk studies [19]. These studies commonly integrate thermal environment information with census, demographic, socioeconomic, or healthcare-related indicators. Existing HHRI studies have been conducted at multiple spatial levels. At the regional or national scale, studies usually adopt a macro perspective, assessing heat health risk across countries, regions, or cities. This approach supports broad disaster-prevention planning and regional resource allocation. For example, Estoque et al. (2020) assessed heat health risk across 139 Philippine cities [20]. Thakkar et al. (2025) evaluated heat health risk across cities in Karnataka, India [21]. Wu et al. (2024) conducted a comprehensive assessment of heat health risk in the Yangtze River Delta, China [22]. At the urban or intra-urban scale, studies usually focus on finer spatial

units within individual cities. These analyses use more detailed urban data, such as population distribution, healthcare accessibility, land cover, and built-environment indicators. They can reveal spatial heterogeneity that is hidden in regional assessments. Zha et al. (2024) assessed street-level heat health risk in Beijing and further examined the role of green infrastructure [23]. Wang et al. (2023) evaluated heat health risk at the census-unit scale across eight Australian cities [24]. Several studies have also used the Local Climate Zone (LCZ) classification [25], linking urban morphology with heat-related risk. For example, Baqa et al. (2025) combined LCZ classification with census wards and analyzed heat health risk across different LCZ types in Karachi, Pakistan [26]. By integrating thermal environment observations with socioeconomic conditions and infrastructure characteristics, these studies have provided valuable insights for heat health risk assessment.

Despite these advances, several gaps remain in current heat health risk studies. First, macro- and fine-scale assessments are often developed separately. Regional or administrative-level studies can reveal broad spatial patterns, whereas intra-urban studies can capture finer spatial heterogeneity. However, a systematic framework that links regional screening with within-city diagnosis remains insufficient. This limits the translation from broad risk identification to fine-scale intervention. Second, although nighttime heat has been shown to impose substantial health impacts, studies focusing specifically on nighttime heat health risk remain limited [17]. A key constraint is the spatial resolution of nighttime thermal observations. Existing thermal products often lack sufficient detail for block-level assessment within cities at night [27]. Third, urban morphology has been increasingly recognized as an important factor shaping urban thermal environments and heat health risk. The LCZ framework provides a standardized basis for linking urban form with thermal conditions [25]. However, most LCZ-based studies focus on differences in risk levels across LCZ types [28–30]. Few studies examine whether hazard, exposure, or vulnerability dominates heat health risk under different urban forms. This limits their value for designing differentiated adaptation strategies.

To address these gaps, this study develops a multi-scale framework for nighttime heat health risk assessment in Shandong Province, China. At the macro scale, district-level HHRI is calculated by integrating MODIS nighttime LST with socio-statistical data. Hotspot analysis is then used to identify statistically significant high-risk clusters and select representative cities for fine-scale assessment. At the fine scale, the Sustainable Development Science Satellite 1 (SDGSAT-1) nighttime thermal observations are integrated with socioeconomic, demographic, infrastructure, and built-environment data to assess block-level HHRI [31,32]. Dominant-factor diagnostics are conducted for spatial units at both scales, based on the classified hazard, exposure, and vulnerability components [33,34]. These diagnostics are further linked with LCZ classification at the block scale, to examine how dominant risk structures vary across urban morphological contexts. Specifically, this study aims to (1) clarify the spatial distribution and clustering characteristics of nighttime heat health risk across districts in Shandong Province; (2) characterize fine-scale intra-urban risk patterns in selected high-risk cities; and (3) identify dominant risk factors at both scales and examine their associations with LCZ types at the block scale.

Through this design, the study makes three main contributions. First, it connects regional risk screening with intra-urban diagnosis, providing a continuous pathway from priority-area identification to block-level interpretation. Second, it extends high-resolution nighttime thermal remote sensing to heat health risk assessment, using SDGSAT-1 observations to capture block-scale heat-hazard heterogeneity. Third, it advances LCZ-based heat-risk analysis from risk-level comparison toward dominant-factor interpretation. By identifying whether hazard, exposure, vulnerability, or their combinations dominate within

different urban forms, the framework provides more actionable evidence for differentiated heat adaptation.

2. Study Area and Datasets

2.1. Study Area

This study focuses on Shandong Province in eastern China (114°47′–122°42′E, 34°22′–38°23′N) (Figure 1). Shandong has a temperate monsoon climate with hot summers and frequent extreme heat events. In recent decades, rapid urbanization and land-use change have intensified urban thermal environments and strengthened urban heat island effects across many cities, making nighttime heat and its associated health risks an increasing concern in the province.

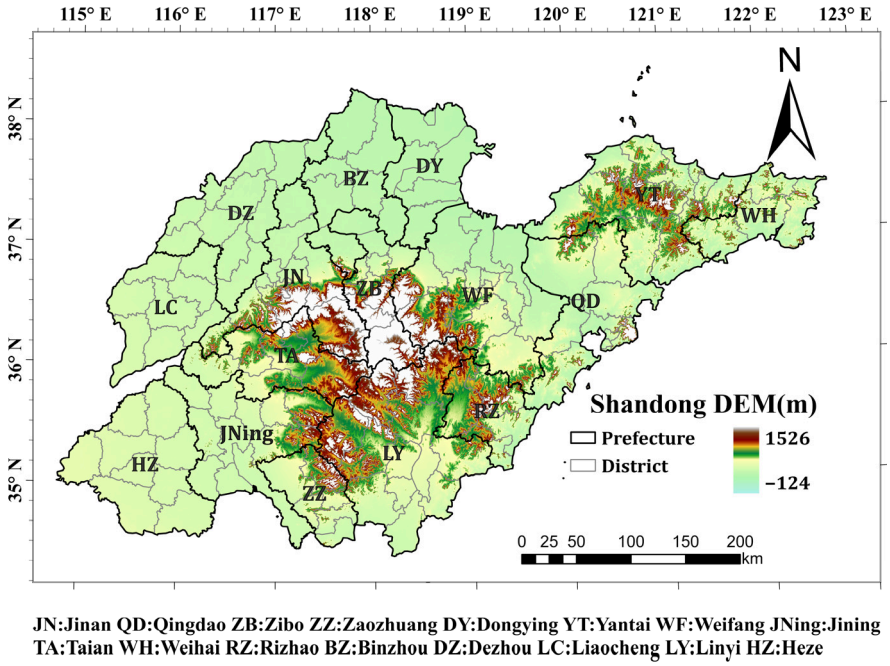

Figure 1. The map of Shandong province.

2.2. Datasets

This study integrates remote sensing, socio-statistical, population, LCZ, and infrastructure-related datasets for multi-scale heat health risk assessment. At the macro scale, MODIS nighttime LST and VIIRS/DNB data were used, while SDGSAT-1 and Landsat 8 data were employed at the fine scale. Socio-statistical and geo-information datasets included district-level census data, WorldPop population data, medical accessibility data [35], LCZ data [36], and block division data [37]. The datasets used in this study are shown in Table 1.

All spatial datasets were transformed into a common coordinate system before integration. At the macro scale, MODIS LST rasters were converted to points and spatially joined to district polygons. The mean LST value within each district was calculated to represent heat hazard. Census-based socioeconomic and population indicators were linked to districts through attribute-table joins. At the fine scale, raster datasets were resampled to match the 30 m resolution of SDGSAT-1 data, converted to points, and spatially joined to urban block polygons. Mean raster values were then assigned to each block. The selected SDGSAT-1 scenes were cloud-free over the study areas, and no-data pixels were excluded during spatial aggregation.

Table 1. Datasets used in this study.

Data	Scale	Resolution	Description	Source
MOD11A1	District	1 km	Land Surface Temperature (LST)	MODIS/061/MOD11A1
VIIRS/DNB	District	500 m	Night Light Intensity (NLI)	NOAA/VIIRS/DNB/ MONTHLY_V1/VCMSLCFG
Statistical Data	District	/	Data on economy, housing, etc	http://tjj.shandong.gov.cn/pcsj/2020/zk (accessed on 25 August 2025)
Population	Block/District	100 m	Population distribution	https://hub.worldpop.org/ (accessed on 1 September 2025)
SDGSAT-1	Block	30 m	LST and NLI	https://www.sdgsat.ac.cn./ (accessed on 12 September 2025)
Landsat 8	Block	30 m	EVI; NDBI; MNDWI	LANDSAT/LCO8/C02/T1 L2
LCZ	Block	100 m	Confirm the LCZ classification of the block	https://doi.org/10.5281/zenodo.6364594
Accesibility	Block	1 km	Accessibility of medical facilities	https://doi.org/10.6084/m9.figshare.c.7318976
Block division	Block	/	Precise delineation of urban blocks	https://doi.org/10.6084/m9.figshare.26021314

3. Methodology

We developed a multi-scale framework for heat health risk assessment (Figure 2). The analytical procedure consists of four main steps: (1) heat health risk was assessed at the district level across Shandong Province to characterize the macro-scale spatial pattern; (2) hotspot analysis was applied to identify statistically significant clusters of high-risk districts; (3) high-risk cities located within statistically significant hotspot clusters were selected based on the macro-scale results and further examined at the block level; and (4) dominant risk factors were identified for each spatial unit and integrated with LCZ data to examine the relationship between urban morphology, risk distribution, and dominant risk drivers.

3.1. Heat Health Risk Assessment

Following Crichton's risk triangle, this study assesses heat health risk as the combined outcome of hazard, exposure, and vulnerability. The heat health risk index (HHRI) was therefore constructed using a multiplicative model, as shown in Equation (1).

$$\mathrm{HHRI} = \sqrt[3]{\mathrm{H} \times \mathrm{E} \times \mathrm{V}} \quad (1)$$

where HHRI denotes the heat health risk index, and H, E, and V represent the heat hazard index, heat exposure index, and heat vulnerability index, respectively. The three components were assigned equal weight. Previous studies have adopted a variety of weighting approaches for heat health risk assessment, including equal weighting [29,38–40], PCA [41], entropy weighting [42,43], CRITIC [44], and probabilistic models [45]. This study adopted equal weighting to maintain consistency between composite HHRI assessment and dominant-factor diagnosis, the latter being based on independent classifications of hazard, exposure, and vulnerability.

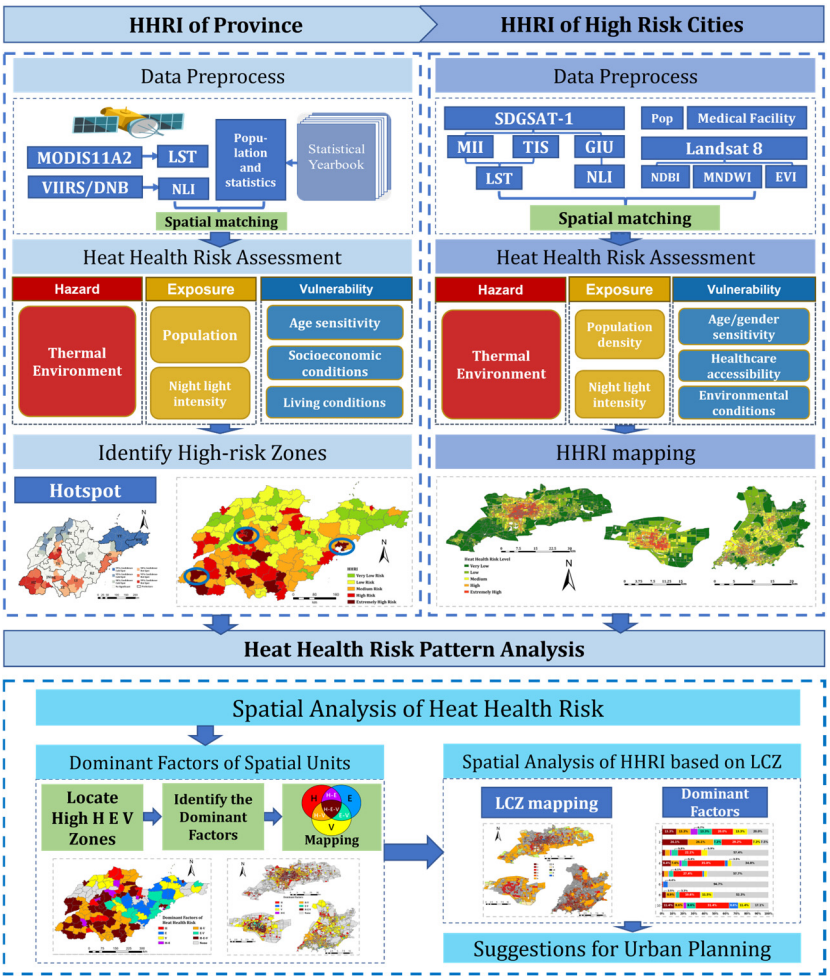

Figure 2. Research framework of this study.

To ensure comparability among indicators and enable subsequent aggregation, all variables were standardized before calculation. Positive indicators, for which higher values indicate greater risk, were normalized using Equation (2), whereas negative indicators were standardized using Equation (3). This treatment preserves the directional meaning of each indicator and avoids zero or negative values in subsequent calculations [23,46]. The 0.1–0.9 normalization range was used to avoid zero values in the multiplicative HHRI model. This adjustment prevents extremely low component values from forcing HHRI to zero, while retaining sensitivity to high-risk extremes [47].

$$X' = 0.1 + \frac{X - X_{min}}{X_{max} - X_{min}} \times (0.9 - 0.1) \quad (2)$$

$$X' = 0.1 + \frac{X_{max} - X}{X_{max} - X_{min}} \times (0.9 - 0.1) \quad (3)$$

where X' is the standardized value (range 0.1~0.9) and X is the original value. X_{max} and X_{min} are the maximum and minimum values of the original data.

3.1.1. Heat Hazard

Heat hazard represents the thermal stress imposed by environmental heat conditions and forms the physical basis of heat-related health risk. In this study, LST was used as the core indicator of heat hazard because remotely sensed LST is strongly correlated with near-surface air temperature and can capture spatial variations in urban thermal conditions [48–50]. Nighttime LST was used to characterize heat hazard at both

scales, with MODIS LST applied to district-level assessment and SDGSAT-1 LST applied to block-level assessment.

3.1.2. Heat Exposure

Heat exposure refers to the population potentially affected by high-temperature conditions. In this study, population and NLI were used to characterize heat exposure. Specifically, population represents the residential population distribution [51], whereas NLI reflects nighttime human activity beyond residential areas [52]. The population indicator differed across scales. At the macro scale, total population was used because district-level population density can be strongly affected by differences in administrative area and land-use composition [53]. At the fine scale, population density was used to capture the intensity of population aggregation within urban blocks and to reduce the influence of unit size [54]. The heat exposure index was calculated by combining population indicators with NLI, as shown in Equation (4).

$$\text{Exposure} = \text{Pop} + \text{NLI} \quad (4)$$

where Pop represents population, expressed as total population at the macro scale and population density at the fine scale, and NLI denotes nighttime light intensity.

3.1.3. Heat Vulnerability

Heat vulnerability reflects susceptibility to adverse health outcomes under high-temperature conditions. In this study, vulnerability indicators differed between the macro and fine scales because of data availability and spatial analytical needs. The indicators used at the two scales are listed in Table 2.

Table 2. Vulnerability indicators used at the macro and fine scales.

Scale	Dimension	Indicator	Direction
Macro	Demographic sensitivity	Population under 15 years old	Positive
		Population over 65 years old	Positive
	Socioeconomic status	Low education level	Positive
		High-risk occupations	Positive
	Living conditions	Single-person households	Positive
		Households without tap water	Positive
		Households without bathing facilities	Positive
Fine	Demographic sensitivity	Population under 15 years old	Positive
		Population over 65 years old	Positive
		Female population density	Positive
	Medical accessibility	Travel time to the nearest medical facility	Positive
	Built-environment conditions	NDBI	Positive
		NDVI	Negative
		MNDWI	Negative

At both scales, populations under 15 years old and over 65 years old were included. These groups represent thermally sensitive populations [55–57]. At the macro scale, vulnerability was characterized by demographic sensitivity, socioeconomic status, and living conditions. At the fine scale, vulnerability was characterized by demographic sensitivity, medical accessibility, and built-environment conditions. NDVI and MNDWI were treated

as negative indicators, because higher values generally indicate lower heat vulnerability. Heat vulnerability was then calculated using Equation (5):

$$\text{Vulnerability} = \sum_{i=1}^{7} V_i \tag{5}$$

where V_i represents the heat vulnerability indicator at the corresponding scale. The same number of indicators is used at both scales.

3.2. Hotspot Analysis

Hotspot analysis based on the Getis–Ord Gi* statistic is used to identify spatial clustering of heat health risk across districts in Shandong Province. The Gi* statistic evaluates local spatial association by comparing the value of each spatial unit with those of its neighboring units, thereby identifying statistically significant clusters of high values (hotspots) and low values (cold spots) [58]. The Gi* statistic is calculated as follows:

$$Gi^* = \frac{\sum_{j=1}^{n} w_{i,j}x_j - \overline{X}\sum_{j=1}^{n} w_{i,j}}{S\sqrt{\frac{n\sum_{j=1}^{n} w_{i,j}^2 - \left(\sum_{j=1}^{n} w_{i,j}\right)^2}{n-1}}} \tag{6}$$

$$\overline{X} = \frac{\sum_{j=1}^{n} x_j}{n} \tag{7}$$

$$S = \sqrt{\frac{1}{n}\sum_{j=1}^{n} x_j^2 - \left(\overline{X}\right)^2} \tag{8}$$

where x_j represents the attribute value for feature j, and $w_{i,j}$ is the spatial weight defined using a k-nearest neighbor (KNN) approach based on Euclidean distance. Districts identified as hotspots at the 95% and 99% confidence levels were extracted as priority areas for subsequent fine-scale analysis. This approach allows the fine-scale assessment to focus on statistically significant clusters of high-risk areas.

3.3. Retrieval of Land Surface Temperature

In this study, LST retrieval is conducted for the fine-scale analysis based on SDGSAT-1 TIS data using the split-window algorithm (SWA). The SWA exploits the differential absorption of atmospheric water vapor in two adjacent thermal infrared channels (bands 2 and 3) to reduce atmospheric effects [59]. By using the brightness temperature difference between these channels, together with surface emissivity and atmospheric water vapor content, LST can be estimated without requiring detailed atmospheric profile data [60]. The split-window formulation is expressed as follows:

$$T_s = TB_2 + C_1(TB_2 - TB_3) + C_2(TB_2 - TB_3)^2 + C_0 + (C_3 + C_4W)(1 - m) + (C_5 + C_6W)\triangle m - 273.15 \tag{9}$$

where T_s is land surface temperature (°C); TB_2 and TB_3 are the brightness temperatures of TIS bands 2 and 3, respectively; m is the mean emissivity of two bands; $\triangle$m is the difference in land surface emissivity; W is atmospheric water vapor content (g*cm^{-2}); and C_0~C_6 are algorithm coefficients [61]. The values of these coefficients are listed in Table 3.

Table 3. Split-window coefficient values of this study.

Constant	C_0	C_1	C_2	C_3	C_4	C_5	C_6
Value	−0.268	1.378	0.183	54.300	−2.238	−129.200	16.400

To implement the retrieval, the digital number (DN) values of the thermal infrared bands were first converted to top-of-atmosphere (TOA) spectral radiance through radiometric calibration:

$$L_\lambda = \left(\frac{L_{max} - L_{min}}{DN_{max}}\right) \times DN + L_{min} \quad (10)$$

where L_λ is the TOA radiance in ($W \times m^{-2} \times sr^{-1} \times \mu m^{-1}$), L_{max} and L_{min} are band-specific calibration parameters. The radiance was then converted to brightness temperature using Planck's law:

$$TB = \frac{K_2}{\ln\left(\frac{K_1}{L_\lambda} + 1\right)} \quad (11)$$

where TB is the brightness temperature, K_1 and K_2 are band-specific thermal constants obtained from the metadata. Land surface emissivity (LSE) was estimated from SDGSAT-1 MII data using the normalized difference vegetation index (NDVI) threshold method. NDVI, fractional vegetation cover (FVC), and LSE were calculated as follows:

$$NDVI = \frac{NIR - RED}{NIR + RED} \quad (12)$$

$$FVC = \left(\frac{NDVI - NDVI_{soil}}{NDVI_{veg} - NDVI_{soil}}\right)^2 \quad (13)$$

$$LSE = \varepsilon_{soil} \times (1 - FVC) + \varepsilon_{veg} \times FVC \quad (14)$$

where NIR and RED are bands 7 and 5 of SDGSAT-1 MII data, respectively. $NDVI_{soil}$ is the NDVI value of bare soil, and $NDVI_{veg}$ is the NDVI value of vegetation. ε_{soil} and ε_{veg} are emissivity of the soil and vegetation. The emissivity parameters required by the split-window algorithm were then derived as the mean emissivity and emissivity difference between bands 2 and 3:

$$m = \frac{LSE_2 + LSE_3}{2} \quad (15)$$

$$\triangle m = LSE_2 - LSE_3 \quad (16)$$

Atmospheric water vapor content was estimated using the multi-year mean from meteorological observations. Finally, brightness temperature, emissivity parameters, and atmospheric water vapor content were substituted into Equation (9) to obtain LST.

3.4. Classification of Risk Levels and Dominant Factors

The HHRI and its components were classified into five levels using the Jenks natural breaks method in ArcGIS Pro 3.4.2: very low, low, medium, high, and very high. The Jenks method determines class breaks from the natural distribution of data values. It groups similar values into the same class and places class boundaries where relatively large value differences occur [62]. Mathematically, it searches for the class partition that minimizes the total within-class variance:

$$\arg\min_{C_1,\ldots,C_k} \sum_{j=1}^{k} \sum_{x_i \in C_j} \left(x_i - \bar{x}_j\right)^2 \quad (17)$$

where x_i is the value of spatial unit i, C_j is class j, $\bar{x}_j$ is the mean value of class j, and k is the number of classes.

At the fine scale, Jenks classification was performed separately for each case city. This avoided biased class assignment across cities with different overall risk levels. For dominant-factor identification, a component classified as high or very high was defined as dominant, whereas a component classified as very low, low, or medium was defined as

non-dominant. The dominant-factor type was then determined according to the number and combination of dominant components, as shown in Table 4.

Table 4. Classification rules for dominant-factor types.

Dominance Category	Type	Explanation
None	None	No dominant component
Single-factor	H	Hazard-dominant
	E	Exposure-dominant
	V	Vulnerability-dominant
Dual-factor	H-E	Dominated by hazard and exposure
	H-V	Dominated by hazard and vulnerability
	E-V	Dominated by exposure and vulnerability
Triple-factor	H-E-V	Dominated by all three components

4. Result

4.1. Macro-Scale Assessment of Heat Health Risk Index and Its Components

4.1.1. Heat Hazard Index

Figure 3a illustrates the spatial distribution of average summer (2022–2024) land surface temperature in Shandong Province. Nighttime LST ranges from approximately 18.22 °C to over 29 °C, indicating pronounced spatial heterogeneity across the province. A clear urban heat island effect is observed in major urban areas. High-temperature zones are mainly concentrated in urban regions and around large water bodies. The highest temperature occurs in the Yellow River Delta. Temperatures there are 2–3 °C higher than those in central urban districts.

The spatial distribution of nighttime heat hazard in Shandong Province exhibits a general pattern of higher values in the northern and southern regions (Figure 3b), with lower levels in the central and peninsula areas. Across the province, from the peninsula coast toward the southwestern inland, heat hazard increases in a clear stepwise pattern. A medium-hazard belt in the central study area aligns closely with the Yellow River's course, indicating that the river's heat capacity and associated moisture transport significantly warm the nighttime environment along its banks, forming a distinct thermal corridor.

4.1.2. Heat Exposure Index

The spatial distribution of nighttime heat exposure in Shandong Province shows a distinctly discrete pattern (Figure 3c). A total of 16 districts are classified as high exposure and 11 (8.09%) as very high exposure, mainly concentrated in the built-up districts of prefecture-level cities. In contrast, districts with lower exposure are mainly found in the northern, northwestern, and northern Jiaodong Peninsula districts. Overall, nighttime heat exposure is primarily shaped by urbanization and population concentration.

4.1.3. Heat Vulnerability Index

The spatial pattern of nighttime heat vulnerability in Shandong Province shows clear regional differentiation, with higher vulnerability in the southern regions (Figure 3d). Two primary high-value cores are identified in the southern part of the province. One is centered within Heze City, indicating widespread high vulnerability, while the other spans the junction of Jining, Linyi, and Zaozhuang cities, forming a trans-administrative high-value cluster. These two areas highlight the concentration of extreme vulnerability in southern Shandong. In contrast, central and Shandong Peninsula areas exhibit predomi-

nantly medium to low vulnerability, with fewer high vulnerability districts scattered across these areas.

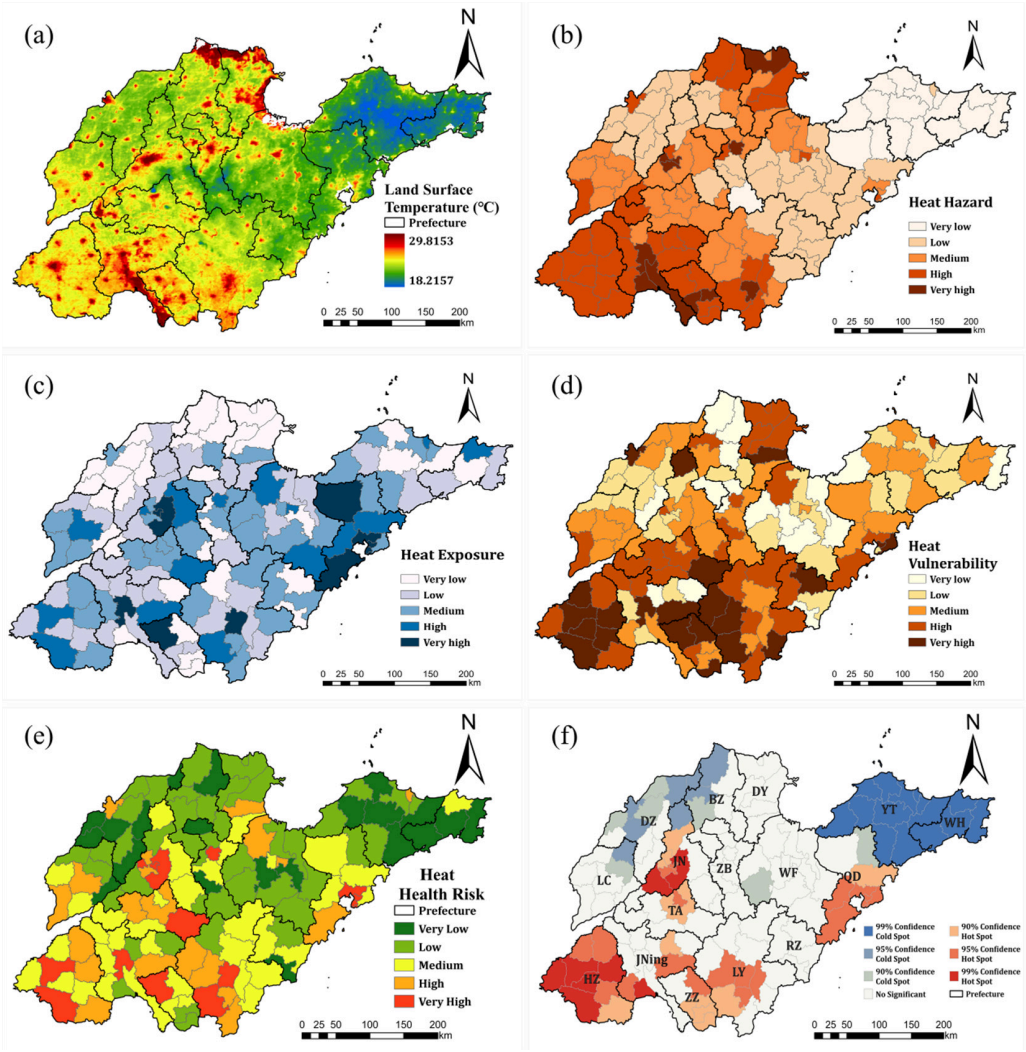

Figure 3. Heat health risk results of Shandong province. (**a**) Nighttime LST. (**b**) Heat hazard. (**c**) Heat exposure. (**d**) Heat Vulnerability. (**e**) Heat health risk. (**f**) Hotspot.

4.1.4. Heat Health Risk Index

The nighttime heat health risk index was calculated by integrating the standardized values of heat hazard, heat exposure, and heat vulnerability (Figure 3e). A total of 15 districts (11.03%) were classified as very high risk, and 20 districts (14.71%) as high risk. In addition, 37 districts (27.21%), 43 districts (31.62%), and 21 districts (15.44%) were classified as medium, low, and very low risk, respectively.

Notably, all very high-risk districts were located in central urban areas, highlighting the concentration of nighttime heat health risk in major urban cores. In Dezhou and Zibo, for example, districts covering the central urban area exhibited markedly higher nighttime risk levels than surrounding districts, forming a clear center–periphery contrast. Most very high-risk districts were concentrated in large and more developed cities. Nearly half of these districts were located in Qingdao and Jinan. Nevertheless, very high-risk districts also occurred in less developed cities, particularly in southwestern Shandong.

Medium-risk districts were concentrated mainly in the southern and central parts of Shandong Province. Low-risk and very low-risk districts were distributed predominantly across the central-northern part of the province. Yantai and Weihai, on the Shandong Peninsula, formed the main concentration area of very low-risk districts. Taken together,

the spatial pattern of nighttime heat health risk in Shandong Province was characterized by higher risk in the south and lower risk in the north.

4.1.5. Hot Spot Analysis

The results of hotspot analysis show that heat health risk in Shandong Province exhibits statistically significant hot spots and cold spots (Figure 3f). Large areas of the province show no significant clustering, indicating that high-risk values are concentrated only in specific regions.

Hotspots are concentrated mainly in the southern part of Shandong Province and form several distinct cores. Southwestern Shandong, particularly the entire administrative area of Heze City, constitutes the most concentrated hotspot region, with a confidence level of 99%. Jinan and Tai'an form another hotspot core, with confidence levels ranging from 95% to 99%. In the southern Shandong Peninsula, Qingdao and its surrounding areas constitute a relatively independent hotspot cluster, with confidence levels comparable to those in southwestern Shandong. This indicates that risk aggregation occurs not only in inland areas but also in coastal metropolitan regions. Cold spots are concentrated in Yantai and Weihai on the Shandong Peninsula, where they form a continuous cold spot region.

4.2. Fine-Scale Assessment of Heat Health Risk Index and Its Components

Following the macro-scale risk patterns identified in Shandong Province, three representative high-risk cities were selected as case studies (Figure 4). These cities were further examined at the block level to reveal the fine-scale spatial patterns of urban heat health risk. Among them, Jinan shows the highest nighttime thermal intensity. Its maximum land surface temperature exceeds 38 °C, and the urban–rural thermal contrast is more than 20 °C. In Qingdao and Heze, the maximum nighttime temperatures are both only slightly above 30 °C, as detailed in Table 5.

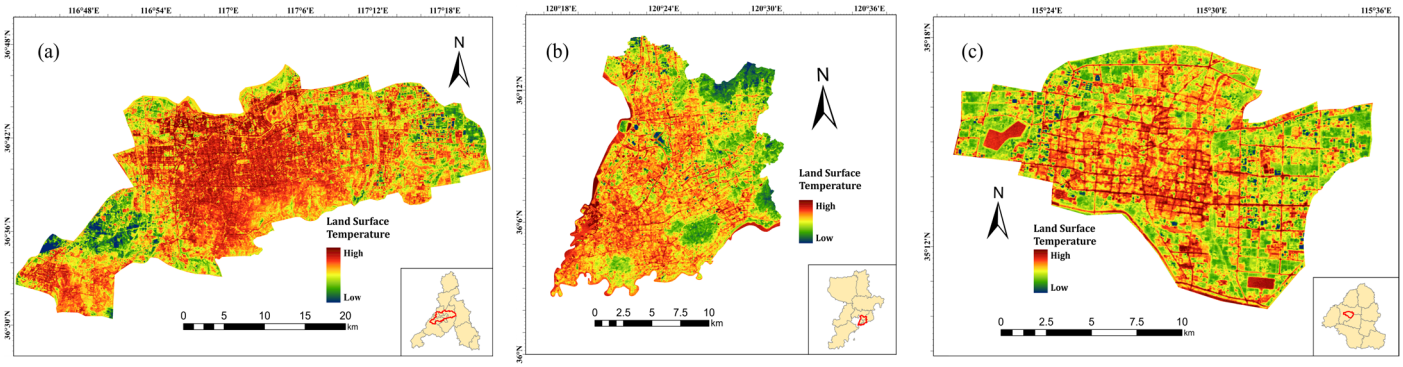

Figure 4. Case cities' LST from SDGSAT-1. (**a**) Jinan. (**b**) Qingdao. (**c**) Heze.

Table 5. Acquisition dates and meteorological background of SDGSAT-1 TIS scenes used in the fine-scale analysis.

Cities	Date	Daily Air Temperature (T_{max}/T_{min}, °C)	Land Surface Temperature (T_{max}/T_{min}, °C)	Meteorological Background
Jinan	23 June 2023	40/27	38/15	Extreme heat during heatwave period
Qingdao	29 August 2024	31/24	30/14	Locally high-temperature summer condition
Heze	22 August 2024	35/26	31/14	Extreme heat during heatwave period

4.2.1. Heat Hazard Index

Heat hazard differs clearly among the three cities at the block level (Figure 5a–c). Jinan has the highest share of high and very high hazard blocks, reaching 62.31%, followed by Qingdao at 45.49% and Heze at 41.21%. This indicates that heat hazard is strongest in Jinan.

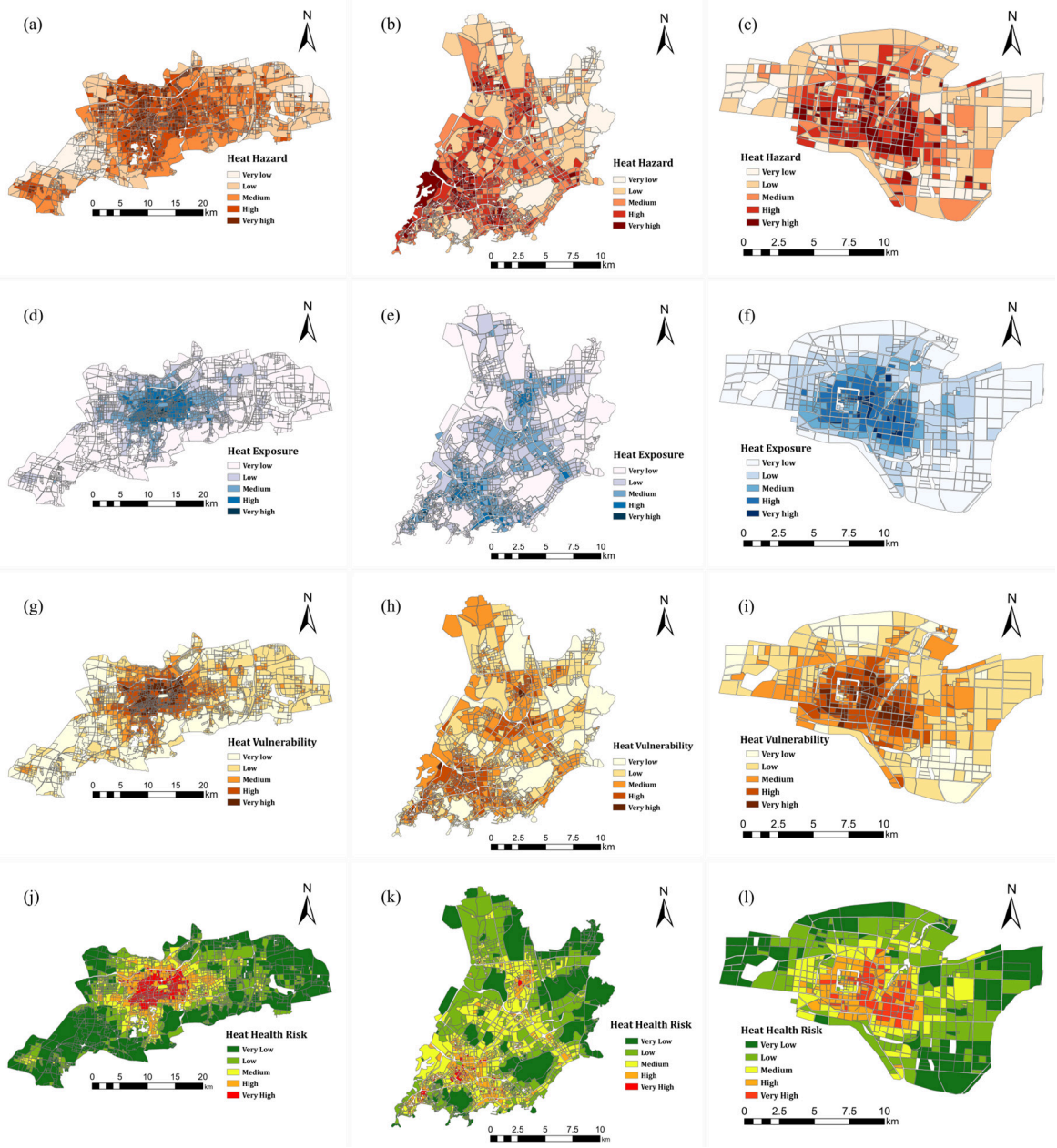

Figure 5. Heat health risk and its components in three cities. Heat hazard of (**a**) Jinan, (**b**) Qingdao, (**c**) Heze; heat exposure of (**d**) Jinan, (**e**) Qingdao, (**f**) Heze; heat vulnerability of (**g**) Jinan, (**h**) Qingdao, (**i**) Heze; heat health risk of (**j**) Jinan, (**k**) Qingdao, (**l**) Heze.

Jinan shows a highly centralized and continuous high-hazard pattern, with dense clusters around Daming Lake and an additional hotspot near Jinan West Railway Station. Qingdao presents a fragmented and polycentric structure, with high-hazard clusters near Qingdao Port and in the central districts of Shibei and Shinan. Heze shows a weaker but still evident central clustering pattern, with very high hazard blocks mainly located between the Zhaowang River and Heze Railway Station.

4.2.2. Heat Exposure Index

Nighttime heat exposure at the block level differs clearly among the three cities (Figure 5d–f). Heze has the highest share of high- and very high-exposure blocks, reaching 27.35%. Jinan follows with 22.96%, while Qingdao has the lowest share at 15.72%.

The three cities also differ in their spatial patterns of exposure. In Jinan, high-exposure blocks show a pronounced concentration in the urban center. Very high-exposure blocks are particularly concentrated in the southwestern old urban area. Qingdao displays a fragmented and polycentric pattern. Several small clusters of high exposure are linked by medium-exposure blocks, while low- exposure areas are mainly located in coastal and mountainous zones. Heze shows a relatively regular center-periphery structure. High exposure is concentrated in the urban core and gradually declines toward the outskirts.

4.2.3. Heat Vulnerability Index

Heat vulnerability differs clearly among the three cities at the block level (Figure 5g–i). In Jinan, high- and very high-vulnerability blocks account for 32.15% of the total. The corresponding proportion is 28.73% in Qingdao and 33.57% in Heze. This indicates that vulnerability is relatively higher in Heze and Jinan.

In terms of spatial distribution, very high-vulnerability blocks form a southwest–northeast belt in Jinan, concentrated mainly in the southwestern urban area. High-vulnerability blocks are found around this belt. In Qingdao, high- and very high-vulnerability blocks are concentrated mainly in the southern urban area, with smaller clusters in the north. Low vulnerability is more common in coastal and mountainous areas. As for Heze, very high-vulnerability blocks are concentrated in the urban core and are surrounded by high-vulnerability zones, while medium- and low-vulnerability blocks dominate the outer urban area.

4.2.4. Heat Health Risk Index

Heat health risk at the block level varies clearly across the three cities (Figure 5j–l). Jinan has the highest share of high- and very high-risk blocks, reaching 35.93%, followed closely by Heze at 33.57%. Qingdao is lower at 26.82%. Medium-risk blocks are most prominent in Qingdao, where they account for 37.72%, compared with 23.27% in Heze and 19.36% in Jinan. Low- and very low-risk blocks make up 44.71% in Jinan, 43.16% in Heze, and 35.47% in Qingdao.

Jinan shows the strongest concentration of heat health risk in the central urban area. Very high-risk blocks are clustered mainly in the old city west of Daming Lake, especially in the southwestern part, while high-risk blocks extend outward around these cores. Qingdao presents a more dispersed and polycentric pattern. High-risk clusters appear in the northern, southern, and southwestern parts of the city, and very high-risk blocks are embedded within them. The most notable concentrations are found near the commercial area around Taidong Metro Station and along the commercial street east of Qingdao Railway Station. Heze exhibits a clear center–periphery gradient. High- and very high-risk blocks are concentrated in the urban core. Major clusters are located in and around the old urban area within Huandi Park. This high-risk area extends eastward to the area between the Zhaowang River and Heze Railway Station.

Among the three cities, heat health risk is highest in Jinan, while Heze remains close to Jinan despite its smaller urban size. Qingdao has a smaller share of high-risk blocks and a much larger proportion of medium-risk blocks.

4.3. Dominant Factor of Heat Health Risk

4.3.1. Macro-Scale Dominant Factor

The spatial distribution of dominant factors of heat health risk in Shandong Province exhibits a clear regional differentiation (Figure 6a). Overall, dominant factor patterns can be broadly divided into two groups: those involving heat hazard and those independent of heat hazard. The former is mainly distributed along the Yellow River corridor, the Yellow River Delta, and southwestern Shandong, forming several contiguous clusters. In contrast, the latter is primarily concentrated in the Shandong Peninsula, where relatively lower nighttime temperatures reduce the influence of thermal hazard, and heat health risk is more strongly shaped by exposure and vulnerability.

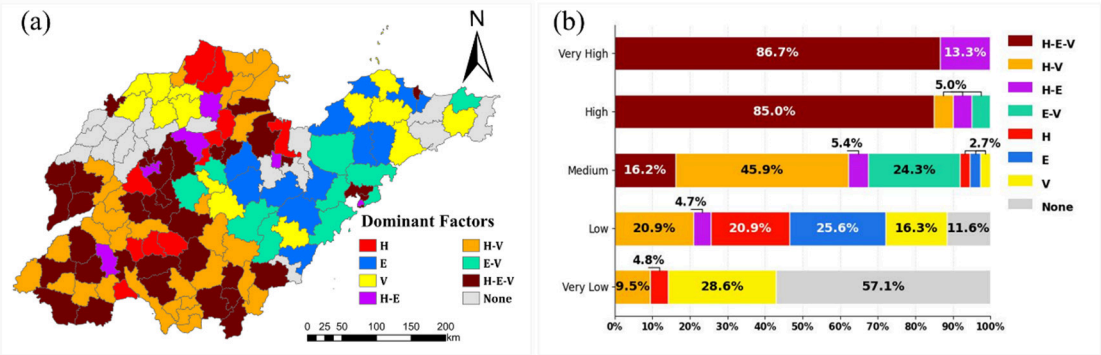

Figure 6. Dominant factors influencing heat-health risk in Shandong Province: (**a**) spatial distribution across districts; (**b**) statistical composition by risk level.

The composition of dominant factor patterns shows a clear gradient across heat health risk levels (Figure 6b). The H-E-V pattern dominates very high- and high-risk districts, accounting for 86.7% and 85.0%, respectively. As risk level decreases, dual- and single-factor dominance become more common, while districts without dominant factors are concentrated mainly in the very low-risk group. This pattern indicates that districts with higher nighttime heat health risk are more likely to be dominated by multiple risk factors.

4.3.2. Fine-Scale Dominant Factor Based on LCZ

To examine how dominant factor patterns vary across urban morphological contexts, built-type LCZs were used to classify urban blocks in Jinan, Qingdao, and Heze. The dominant factor patterns were then analyzed within each LCZ type (Figure 7a,d,g).

The spatial distribution of dominant factors shows a clear intra-urban gradient (Figure 7b,e,h). In all three cities, multiple-dominance patterns are concentrated mainly in central built-up areas, especially in compact and intensive urban forms. In contrast, single-dominance patterns and areas without dominant factors are more frequently distributed in peripheral or less intensively developed blocks.

The LCZ-based results indicate a built-form gradient in dominant factor patterns (Figure 7c,f,i). Under comparable building compactness, multiple dominant factors are more common in blocks with greater overall building height. In Jinan, the proportion of H-E-V dominance reaches 80.2% in LCZ 1 and exceeds 70% in LCZ 2. In Heze, H-E-V dominance in LCZ 2 exceeds 80%. Under comparable building height, multiple dominant factors become less frequent in more open blocks. In LCZ 6, areas without a dominant factor account for more than 70% in Jinan and more than 90% in Qingdao.

Some LCZ types show more heterogeneous dominant factor patterns. LCZ 3, LCZ 5, and LCZ 8 contain a wider range of configurations, including single-, dual-, and triple-dominance patterns. In LCZ 8, patterns involving exposure and vulnerability account for

25–30% in Jinan and more than 20% in Qingdao. These results indicate that the dominant factor structure in these LCZ types varies across blocks rather than being characterized by a single dominant pattern.

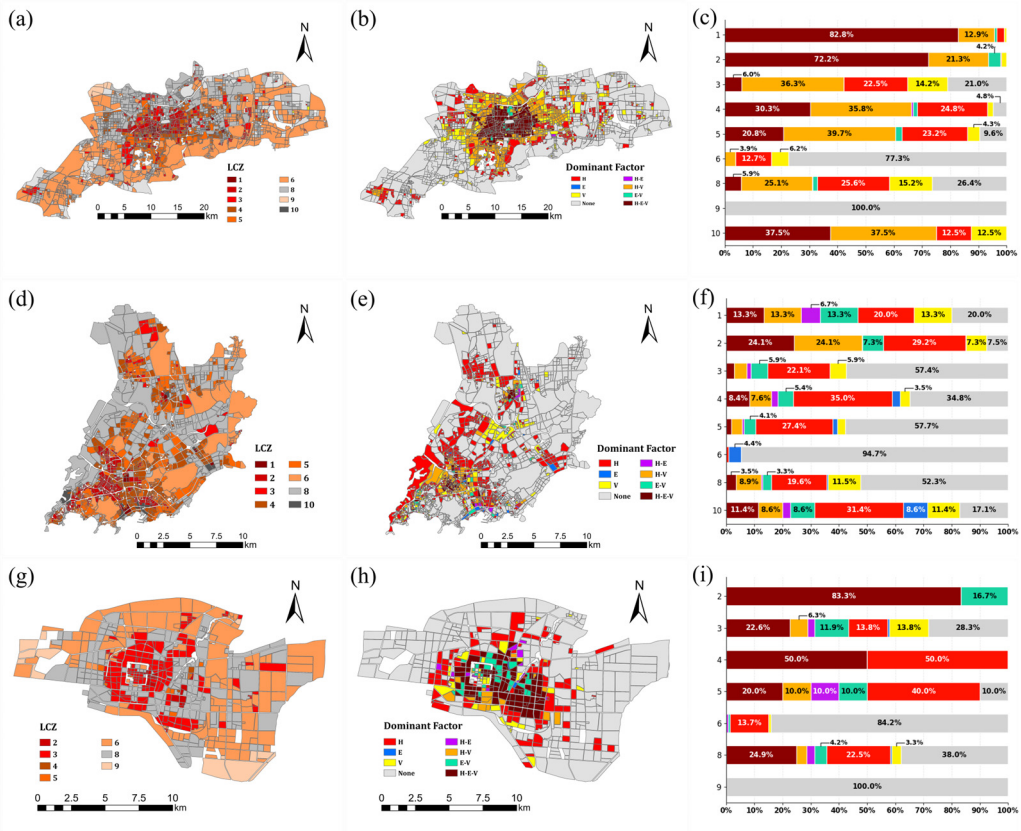

Figure 7. LCZ classification and dominant factor patterns of heat health risk in three cities. (**a**,**d**,**g**) LCZ classification in Jinan, Qingdao, and Heze; (**b**,**e**,**h**) spatial distribution of dominant factors of heat health risk; (**c**,**f**,**i**) composition of dominant factor patterns across LCZ types.

Taken as a whole, the LCZ-based analysis demonstrates that urban morphology is closely associated with both the intensity of heat health risk and the composition of dominant risk factors. As building density and height decrease, dominant factor patterns shift from multi-factor coupling toward simpler configurations. This variation helps distinguish areas requiring comprehensive intervention from those where specific risk components should be prioritized.

5. Discussion

5.1. Advantages of SDGSAT-1 Data in Heat Health Risk Assessment

This study employed SDGSAT-1 thermal infrared data to support fine-scale nighttime heat health risk assessment at the block level. One key advantage of this dataset lies in its stable nighttime observation capability, characterized by consistent overpass timing and wide spatial coverage, which enables the acquisition of spatially continuous imagery within a unified temporal window [31,63]. This feature is particularly important for intra-urban analysis, as it helps reduce potential uncertainties caused by temporal inconsistency [64].

In addition to its temporal stability, SDGSAT-1 provides enhanced capability for capturing fine-scale thermal heterogeneity due to its relatively high spatial resolution (30 m). As illustrated in Figure 8, the LST data from SDGSAT-1 TIS show finer spatial detail than ECO2LSTE, especially in areas with complex road networks, building layouts, and green spaces. This spatial detail supports a more detailed representation of intra-urban

thermal heterogeneity [32,65]. Compared with ECO2LSTE, which has been widely used in urban thermal environment studies, SDGSAT-1 TIS provides a finer depiction of intra-urban LST variability due to its higher spatial resolution. ECO2LSTE provides valuable observations of thermal conditions [30,66–68], while SDGSAT-1 TIS is more suitable for capturing fine-scale spatial variations in dense urban environments [26,27,32].

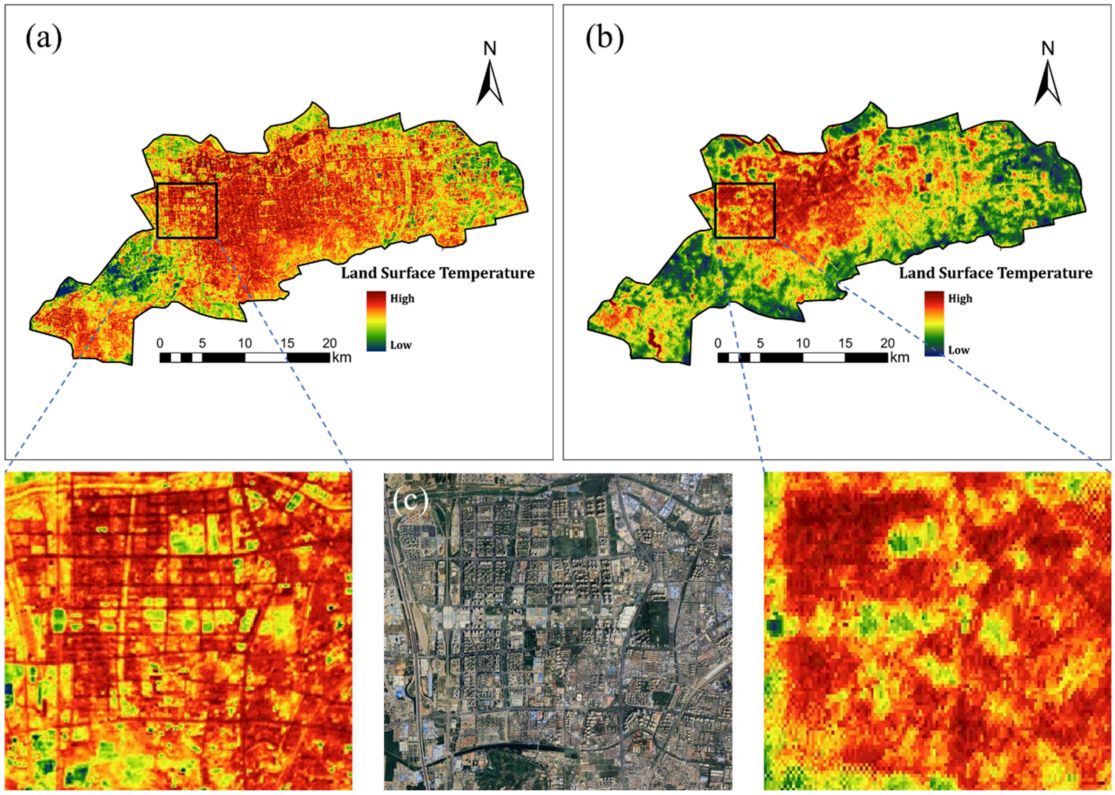

Figure 8. Comparison of LST data from (**a**) SDGSAT-1 TIS and (**b**) ECOSTRESS ECO2LSTE at their native spatial resolutions; (**c**) true-color image of the enlarged area.

Furthermore, the onboard glimmer imager provides nighttime light data at 10 m resolution, which improves the representation of nocturnal human activity [69]. By integrating these data with population distribution, this study enhances the characterization of heat exposure by capturing both residential patterns and activity intensity [52,70]. Together, SDGSAT-1 high-resolution thermal and nighttime light observations support finer urban zoning, bridging broad risk assessment and detailed urban design guidance [71].

5.2. Heat-Related Challenges in Developing Cities

The multi-scale framework developed in this study enables a more systematic identification of heat health challenges in developing cities, such as Heze. By linking province-level screening with block-level analysis, it expands the spatial scope of risk identification beyond major metropolitan and more developed urban areas. Focusing only on large cities may cause other high-risk areas to be overlooked [72]. Under this framework, several small and medium-sized cities with lower levels of development were also identified as high-risk areas. This finding indicates that developing cities warrant greater attention in heat health research. Comparable evidence has also been reported in other studies. Debone et al. (2025) investigated extreme heat and mortality across Brazilian cities of different sizes, including São Paulo as a major metropolitan center, as well as Campinas and Marília as medium-sized and small cities. Their results showed that heat-related mortality was higher in Campinas and Marília than in São Paulo [73]. Similarly, a comparison between Surat,

a medium-sized Indian city studied by Desai et al. (2015), and Delhi, an Indian megacity examined by Kacker et al. (2024), indicates that both cities face severe impacts from high temperatures despite marked differences in scale and development level [74,75]. Pierce et al. (2025) further found that 58 small cities in California generally lacked sufficient capacity to respond to heat-related risks [76]. These studies, consistent with our findings, suggest that developing small and medium-sized cities can experience heat health challenges that are no less severe than those of large metropolitan areas.

Although developing small and medium-sized cities differ from major metropolitan areas in economic level and urban scale, their thermal environments may show similar structural characteristics [77–79]. This indicates that developing cities do not necessarily face weaker thermal stress simply because they are smaller in size. Instead, under comparable thermal conditions, their capacity to respond to heat may be substantially lower [80]. Due to constraints in infrastructure, healthcare services, institutional resources, and public-service provision, developing cities often have weaker heat-response capacity than large metropolitan areas, especially at night [81]. In this sense, the challenge faced by developing cities lies not only in the presence of substantial nighttime heat risk but also in the mismatch between thermal stress and adaptive capacity. This mismatch has important implications for risk governance, because it may deepen inequalities in heat protection and public health support. It is also closely related to sustainable urban development, as improving heat resilience in developing cities is essential for building more equitable, safer, and healthier urban futures.

5.3. Dominant Factor of Heat Health Risk and Its Policy Perspective

In this study, we systematically identified and mapped the dominant factors of heat health risk at both the macro scale and the fine scale. Compared with a single composite heat health risk index, dominant factor analysis provides a more nuanced basis for interpreting spatial heterogeneity. It identifies whether risk in different spatial units is dominated by hazard, exposure, vulnerability, or their combined effects. Such differentiation is important in practice. Even where composite risk levels are similar, dominant risk structures may differ substantially [82]. Different forms of intervention are therefore required. In this way, dominant factor analysis moves heat health risk assessment beyond simple risk mapping and provides a stronger basis for targeted governance and policy design [33].

At both the macro and fine scales, dominant factor configurations show a clear relationship with risk level. At the district scale, very high- and high-risk areas are dominated mainly by the triple-factor H-E-V pattern (Figure 6b). A similar tendency is also observed at the block scale; very high-risk blocks are dominated mainly by the H-E-V configuration, while the overall number of dominant factors declines as risk level decreases (Figure 9). These findings are consistent with previous studies, which have likewise shown that elevated heat health risk is often associated with the joint influence of multiple interacting factors [83].

The LCZ-based results further show that dominant factor configurations differ across urban forms. Within each city, dense and impervious LCZ types showed higher proportions of hazard-dominant blocks, especially where vegetation was limited. This hazard-dominant pattern is consistent with previous findings that paved and sparsely vegetated areas tend to exhibit higher LST [71]. Compact high-rise and compact mid-rise areas, represented by LCZ 1 and LCZ 2, are mainly characterized by multiple dominant factors. By contrast, LCZ 6 and LCZ 9, corresponding to open low-rise and sparsely built areas, more often show no dominant factor. This pattern is consistent with previous LCZ-based heat-risk studies, which found that LCZ 1 and LCZ 2 contain the largest proportions of high and very high risk areas, whereas LCZ 6 and LCZ 9 contain the largest proportions of low and very low

risk areas [26,28,82]. Thus, LCZ classification provides a useful morphological context for interpreting dominant factor configurations.

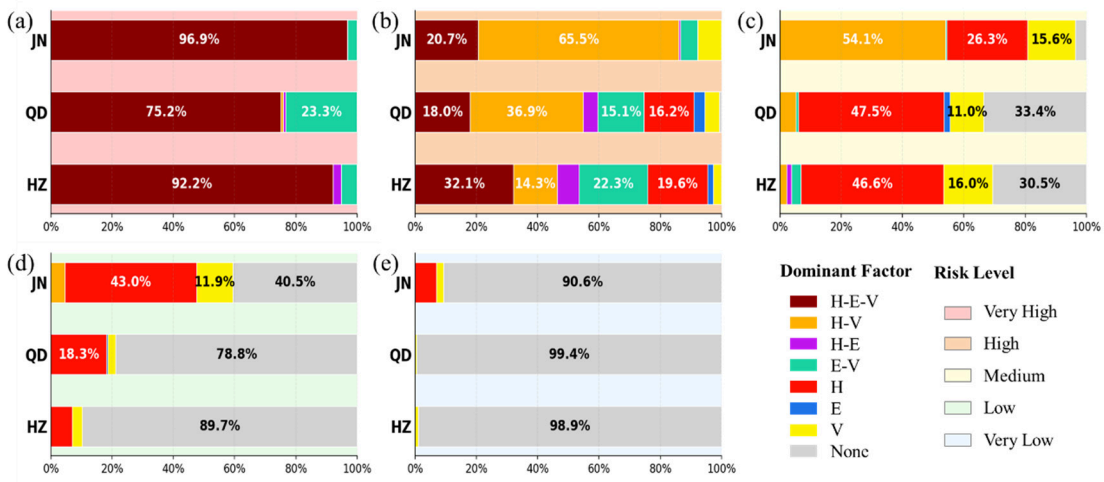

Figure 9. Dominant factor configurations for different heat-health risk levels in Jinan, Qingdao, and Heze: (**a**) very high risk; (**b**) high risk; (**c**) medium risk; (**d**) low risk; (**e**) very low risk.

Dominant factor configurations provide a basis for translating risk assessment into differentiated governance strategies (Figure 10). At the district level, these configurations can be used to determine broad priorities for regional regulation and resource allocation. Districts with hazard-involved configurations should receive earlier attention in nighttime heat monitoring, warning systems, and emergency preparedness [38]. When exposure or vulnerability also participates, resource allocation should further consider the spatial concentration of nighttime activities, medical services, and thermally sensitive populations [84]. Districts without hazard dominance require a more preventive approach, with emphasis on public service capacity, health preparedness, and long-term monitoring of areas where exposure or vulnerability may become critical under future hot-night conditions. At the block level, governance should move from priority setting to site-specific implementation. Dominant factor configurations indicate the main risk dimension to be addressed, while LCZ classification provides the built-form context for selecting feasible measures [28]. In compact and intensive built areas, interventions may focus on roof and pavement albedo, building thermal performance, and ventilation-oriented street or layout adjustment. In blocks where exposure or vulnerability is involved, these physical measures should be coordinated with nighttime activity guidance, service facility placement, medical accessibility, and community-level support.

In this context, the number of dominant factors can serve as an indicator of governance priority. Areas with a greater number of dominant factors usually face more complex risk conditions and therefore require more urgent intervention. Priority should generally be given to areas involving heat hazard, because nighttime thermal stress constitutes the direct environmental basis of heat health risk. Accordingly, governance priority can be broadly ordered as follows: H-E-V, followed by H-E or H-V, and then E-V.

5.4. Limitation and Outlook

This study has several limitations. First, temporal mismatch remains a limitation. The socioeconomic and population data used in this study were derived from the 2020 census. Population changes after 2020 may introduce uncertainty into the assessment results. Future studies should incorporate data that better capture real-time population dynamics, such as mobile phone signaling data and population heat maps [66].

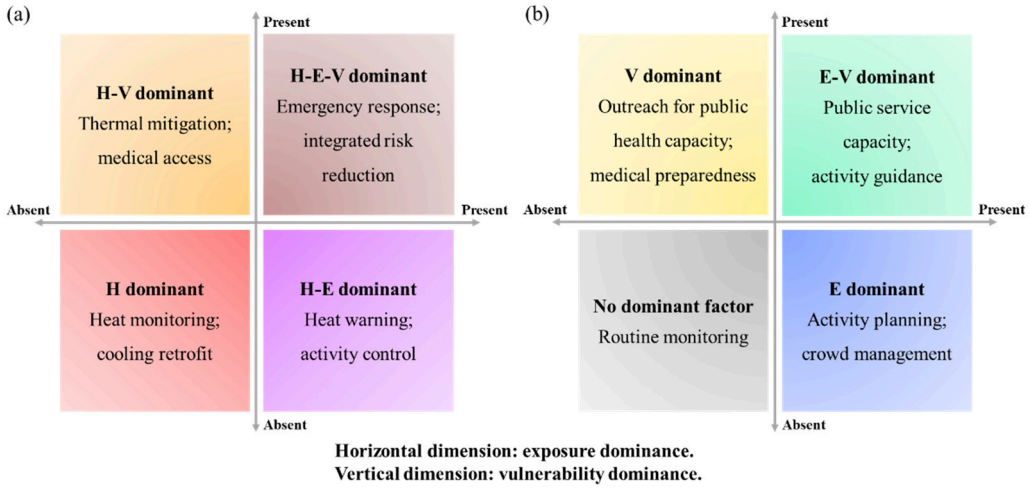

Figure 10. Conceptual governance matrix for nighttime heat health risk: (**a**) response-oriented strategies for hazard-involved configurations; (**b**) prevention-oriented strategies for non-hazard configurations.

Second, public health outcome data were unavailable at the required spatial scale. Therefore, HHRI could not be directly validated against mortality, emergency calls, hospital admissions, or heatstroke records. Future studies should strengthen collaboration with public health agencies and emergency management departments.

Third, indicator-related limitations remain. The use of different indicators across scales reduces the direct comparability of HHRI values between macro- and fine-scale assessments. Equal weighting improves transparency and comparability but may not fully reflect differences in the relative contribution of individual indicators to heat health risk. In addition, although LST is an important indicator of the thermal environment, it may not fully represent human-perceived heat stress. NDVI also cannot fully capture green-space quality, accessibility, or public usability [85]. Future studies should refine both indicator selection and weighting strategies by incorporating human thermal perception metrics [86], more comprehensive green-space indicators, and alternative weighting approaches.

Finally, the effectiveness of specific intervention measures was not evaluated. Future research could combine the proposed strategies with scenario simulations. This would help test how different adaptation measures reduce nighttime heat health risk.

6. Conclusions

This study developed a multi-scale framework for assessing nighttime heat health risk by linking MODIS-based provincial assessment with SDGSAT-1-based block-level analysis. The framework further integrates dominant factor diagnosis with LCZ classification. The main conclusions are as follows:

(1) At the provincial scale, nighttime heat health risk in Shandong Province shows clear spatial heterogeneity. High-risk areas are concentrated mainly in southern Shandong and in the main urban districts of prefecture-level cities.
(2) At the fine scale, inland cities show higher overall nighttime heat health risk than coastal cities. The two inland cities also exhibit similar spatial risk patterns.
(3) At both district and block scales, risk levels are closely associated with dominant factor configurations. Higher-risk units generally involve more dominant factors.
(4) LCZ types are associated with distinct dominant-factor patterns. Multiple dominant factors are more common in taller blocks with similar compactness, but less frequent in more open blocks with similar height.

This approach is also applicable to other regions facing heat-related health risks, especially for identifying less-developed cities. It contributes to more equitable, resilient, and sustainable urban development, aligning with SDG 11.

Author Contributions: Conceptualization, Z.T., Q.M. and B.Z.; methodology, Z.T.; software, Z.T. and C.Z.; validation, C.H. and C.Z.; formal analysis, Q.M., B.Z., P.D., L.L., X.Y. and Z.S.; investigation, Z.T.; resources, Q.M., B.Z., Z.S., L.L. and C.D.; data curation, Z.T., C.H. and C.Z.; writing—original draft preparation, Z.T.; writing—review and editing, Z.T., Q.M., C.H., C.Z., X.S., J.W. and Z.L.; visualization, Z.T.; supervision, Q.M., P.D., B.Z., H.S. and Z.S.; project administration, Q.M., B.Z. and H.S.; funding acquisition, Q.M., B.Z. and H.S. All authors have read and agreed to the published version of the manuscript.

Funding: This work was funded by the National Natural Science Foundation of China (No. 42471363, No. 42171291, No. 42101337), Shandong Province Graduate Teaching Reform Project (SDYJSJGC2024068) and Jinan City-School Integration Project (JNSx2023036).

Data Availability Statement: The datasets generated and/or analyzed during the current study are available from the corresponding author on reasonable request.

Acknowledgments: The research findings are a component of the SDGSAT-1 Open Science Program, which is conducted by the International Research Center of Big Data for Sustainable Development Goals (CBAS). The data utilized in this study is sourced from SDGSAT-1 and provided by CBAS.

Conflicts of Interest: Author Haiying Sun was employed by the company Jinan Rail Transit Group Construction Investment Co., Ltd.. The remaining authors declare that the research was conducted in the absence of any commercial or financial relationships that could be construed as a potential conflict of interest.

References

1. Cheng, Y.; Zhang, Y.; Xu, Y. *Spatio-Temporal Evolution of Regional Carbon Emission Efficiency and the Impact of Technological Innovation*; Beijing Science Press: Beijing, China, 2024.
2. IPCC. *Climate Change 2023: Synthesis Report*; Core Writing Team, Lee, H., Romero, J., Eds.; IPCC: Geneva, Switzerland, 2023.
3. Ebi, K.L.; Capon, A.; Berry, P.; Broderick, C.; de Dear, R.; Havenith, G.; Honda, Y.; Kovats, R.S.; Ma, W.; Malik, A.; et al. Hot weather and heat extremes: Health risks. *Lancet* **2021**, *398*, 698–708. [CrossRef] [PubMed]
4. Epstein, Y.; Yanovich, R. Heatstroke. *N. Engl. J. Med.* **2019**, *380*, 2449–2459. [CrossRef] [PubMed]
5. Martinez-Villalobos, C.; Fu, D.; Loikith, P.C.; Neelin, J.D. Accelerating increase in the duration of heatwaves under global warming. *Nat. Geosci.* **2025**, *18*, 716–723. [CrossRef]
6. Oka, K.; He, J.; Honda, Y.; Hijioka, Y. Economic burden of ambulance transports for patients with heatstroke under climate change: Comparison of the effects of gradual temperature increases and extreme heat events. *Environ. Res. Commun.* **2025**, *7*, 41009. [CrossRef]
7. Chenciner, L.; Cohen, F.; Pouwels, K.B.; Fahr, P.; Perera, R. Associations between extreme heat and hospital length of stay among those hospitalised with cardiovascular disease in Greater London: A population-based longitudinal study between 2007–2019. *Lancet* **2024**, *404*, S25. [CrossRef]
8. Liao, S.; Pan, W.; Wen, L.; Chen, R.; Pan, D.; Wang, R.; Hu, C.; Duan, H.; Weng, H.; Tian, C.; et al. Temperature-related hospitalization burden under climate change. *Nature* **2025**, *644*, 960–968. [CrossRef] [PubMed]
9. Matthews, T.; Raymond, C.; Foster, J.; Baldwin, J.W.; Ivanovich, C.; Kong, Q.; Kinney, P.; Horton, R.M. Mortality impacts of the most extreme heat events. *Nat. Rev. Earth Environ.* **2025**, *6*, 193–210. [CrossRef]
10. Gao, S.; Chen, Y.; Chen, D.; He, B.; Li, K.; Hou, P. More intense and equal compound heatwaves driven by urbanization. *npj Urban Sustain.* **2026**, *6*, 51. [CrossRef]
11. Sun, P.; Yu, S.; Yao, R.; Sun, Z.; Singh, V.P.; Bian, Y.; Ge, C.; Zhang, Q. Urbanization has enhanced compound heatwaves. *J. Geogr. Sci.* **2025**, *35*, 1115–1131. [CrossRef]
12. He, Z.; Wu, Z.; Herzog, O.; Hei, J.; Li, L.; Li, X. Compound health effects and risk assessment of extreme heat and ozone air pollution under climate change: A case study of 731 urban areas in China. *Sustain. Cities Soc.* **2025**, *119*, 106084.
13. Hou, J.; Wang, C.; Wang, H.; Zhang, P. Effects of temperature on mental health: Evidence and mechanisms from China. *China Econ. Rev.* **2023**, *79*, 101953. [CrossRef]

14. Minor, K.; Bjerre-Nielsen, A.; Jonasdottir, S.S.; Lehmann, S.; Obradovich, N. Rising temperatures erode human sleep globally. *One Earth* **2022**, *5*, 534–549. [CrossRef]
15. He, C.; Kim, H.; Hashizume, M.; Lee, W.; Honda, Y.; Kim, S.E.; Kinney, P.L.; Schneider, A.; Zhang, Y.; Zhu, Y.; et al. The effects of night-time warming on mortality burden under future climate change scenarios: A modelling study. *Lancet Planet. Health* **2022**, *6*, e648–e657. [CrossRef] [PubMed]
16. Royé, D.; Sera, F.; Tobías, A.; Hashizume, M.; Honda, Y.; Kim, H.; Vicedo-Cabrera, A.M.; Tong, S.; Lavigne, E.; Kyselý, J.; et al. Short-term association between hot nights and mortality: A multicountry analysis in 178 locations considering hourly ambient temperature. *Environ. Int.* **2025**, *203*, 109719. [CrossRef] [PubMed]
17. Gong, P.; Liu, Q.; Lin, X.; Lin, Y.; Xu, H.; Lan, L. Action on Hot Nights: A Scoping Review of Nighttime Heat Thresholds and Their Critical Role in Urban Climate Resilience. *Sustain. Cities Soc.* **2026**, *142*, 107303. [CrossRef]
18. Crichton, D. The Risk Triangle. In *Natural Disaster Management*; Ingleton, J., Ed.; Tudor Rose: London, UK, 1999.
19. Ye, J.; Yang, F. Towards multi-scale and context-specific heat health risk assessment—A systematic review. *Sustain. Cities Soc.* **2025**, *119*, 106102.
20. Estoque, R.C.; Ooba, M.; Seposo, X.T.; Togawa, T.; Hijioka, Y.; Takahashi, K.; Nakamura, S. Heat health risk assessment in Philippine cities using remotely sensed data and social-ecological indicators. *Nat. Commun.* **2020**, *11*, 1581. [CrossRef] [PubMed]
21. Thakkar, V.; Srinivas, V.; Marula Siddhappanavara, P.; Madappa, T.; Jeganathan, A.; Murthy, I.K. Heatwave health risk index for Karnataka, India. *J. Clim. Change Health* **2025**, *22*, 100428. [CrossRef]
22. Wu, H.; Xu, Y.; Zhang, M.; Su, L.; Wang, Y.; Zhu, S. Spatially explicit assessment of the heat-related health risk in the Yangtze River Delta, China, using multisource remote sensing and socioeconomic data. *Sustain. Cities Soc.* **2024**, *104*, 105300. [CrossRef]
23. Zha, F.; Lu, L.; Wang, R.; Zhang, S.; Cao, S.; Baqa, M.F.; Li, Q.; Chen, F. Understanding fine-scale heat health risks and the role of green infrastructure based on remote sensing and socioeconomic data in the megacity of Beijing, China. *Ecol. Indic.* **2024**, *160*, 111847. [CrossRef]
24. Wang, S.; Sun, Q.C.; Huang, X.; Tao, Y.; Dong, C.; Das, S.; Liu, Y. Health-integrated heat risk assessment in Australian cities. *Environ. Impact Assess. Rev.* **2023**, *102*, 107176. [CrossRef]
25. Stewart, I.D.; Oke, T.R. Local climate zones for urban temperature studies. *Bull. Am. Meteorol. Soc.* **2012**, *93*, 1879–1900. [CrossRef]
26. Baqa, M.F.; Lu, L.; Guo, H.; Song, X.; Alavipanah, S.K.; Nawaz-ul-Huda, S.; Li, Q.; Chen, F. Investigating heat-related health risks related to local climate zones using SDGSAT-1 high-resolution thermal infrared imagery in an arid megacity. *Int. J. Appl. Earth Obs. Geoinf.* **2025**, *136*, 104334. [CrossRef]
27. Ouyang, X.; Sun, Z.; Zhou, S.; Dou, Y. Urban land surface temperature retrieval with high-spatial resolution SDGSAT-1 thermal infrared data. *Remote Sens. Environ.* **2024**, *312*, 114320. [CrossRef]
28. Guo, F.; Fan, G.; Zhao, J.; Zhang, H.; Dong, J.; Ma, H.; Li, N. Urban heat health risk inequality and its drivers based on local climate zones: A case study of Qingdao, China. *Build. Environ.* **2025**, *275*, 112827. [CrossRef]
29. Ma, L.; Huang, G.; Johnson, B.A.; Chen, Z.; Li, M.; Yan, Z.; Zhan, W.; Lu, H.; He, W.; Lian, D. Investigating urban heat-related health risks based on local climate zones: A case study of Changzhou in China. *Sustain. Cities Soc.* **2023**, *91*, 104402. [CrossRef]
30. Ren, Z.; Chen, H.; Sheng, S.; Wang, H.; Zhang, J.; Lu, M. Mapping Multi-Temporal Heat Risks Within the Local Climate Zone Framework: A Case Study of Jinan's Main Urban Area, China. *Buildings* **2025**, *15*, 3619.
31. Guo, H.; Dou, C.; Liang, D.; Jiang, N.; Fu, B.; Han, C.; Chen, F.; Huang, P.; Jing, J.; Zhang, Y.; et al. SDGSAT-1: A Professional Scientific Satellite for Monitoring SDG Indicators. *Proc. IEEE* **2025**, 1–18. [CrossRef]
32. Han, C.; Man, Q.; Dong, P.; Yang, X.; Zhang, B.; Wu, J.; Liu, C.; Zhou, C.; Tan, Z. Exploring the influence of urban morphology on summer daytime and nighttime LST based on SDGSAT-1. *Int. J. Digit. Earth* **2025**, *18*, 2482101. [CrossRef]
33. Huang, H.; Ma, J.; Yang, Y. Spatial heterogeneity of driving factors for urban heat health risk in Chongqing, China: A new identification method and proposal of planning response framework. *Ecol. Indic.* **2023**, *153*, 110449. [CrossRef]
34. Su, R.; Yang, C.; Xu, Z.; Luo, T.; Yang, L. Assessment of Fine-Scale Urban Heat Health Risk and Its Potential Driving Factors Based on Local Climate Zones in Shenzhen, China. *ISPRS Int. J. Geo-Inf.* **2024**, *13*, 367. [CrossRef]
35. Ye, P.; Ye, Z.; Xia, J.; Zhong, L.; Zhang, M.; Lv, L.; Tu, W.; Yue, Y.; Li, Q. National-scale 1-km maps of hospital travel time and hospital accessibility in China. *Sci. Data* **2024**, *11*, 1130. [CrossRef] [PubMed]
36. Demuzere, M.; Kittner, J.; Martilli, A.; Mills, G.; Moede, C.; Stewart, I.D.; van Vliet, J.; Bechtel, B. A global map of local climate zones to support earth system modelling and urban-scale environmental science. *Earth Syst. Sci. Data* **2022**, *14*, 3835–3873. [CrossRef]
37. Tang, J.; Xu, L.; Yu, H.; Jiang, H.; He, D.; Li, T.; Xiao, W.; Zheng, X.; Liu, K.; Li, Y.; et al. A dataset of multi-level street-block divisions of 985 cities worldwide. *Sci. Data* **2025**, *12*, 456. [PubMed]
38. Yang, L.; Yang, C.; Zhou, W.; Liu, L.; Wang, C. Assessing heat-related health risk based on the hazard–exposure–vulnerability framework in Shenzhen, China: A block-level local climate zone perspective. *J. Clean. Prod.* **2025**, *534*, 147036.
39. Xie, Y.; Xu, F.; Ye, Q.; Zhai, Z.; Yang, H.; Feng, X.; Shi, J.; Hu, W. Spatial distribution of old neighborhoods based on heat-related health risks assessment: A case study of Changsha City, China. *Sustain. Cities Soc.* **2024**, *114*, 105740. [CrossRef]

40. Xu, H.; Li, C.; Hu, Y.; Kong, R.; Wang, Q.; Zhou, Y. Long-term temporal and spatial divergence patterns of urban heat risk in the Beijing–Tianjin–Hebei urban agglomeration. *Urban Clim.* **2024**, *56*, 102085.
41. Paranunzio, R.; Dwyer, E.; Fitton, J.M.; Alexander, P.J.; O'Dwyer, B. Assessing current and future heat risk in Dublin city, Ireland. *Urban Clim.* **2021**, *40*, 100983. [CrossRef]
42. Chen, J.; Shi, X.; Shi, Y.; Delina, L.L. Assessing heat vulnerability risk of Jinan and Guangzhou's older populations based on multisource remote sensing data. *Build. Environ.* **2025**, *271*, 112622. [CrossRef]
43. Zou, B.; Fan, C.; Li, J. Quantifying the Influence of Different Block Types on the Urban Heat Risk in High-Density Cities. *Buildings* **2024**, *14*, 2131. [CrossRef]
44. Lan, H.; Zhang, H.; Gao, J.; Bai, J.; Wang, H.; Lu, C.; Geng, H. Heat Risk Assessment in Arid Zones Based on Local Climate Zones: A Case of Urumqi, China. *Buildings* **2025**, *15*, 1672. [CrossRef]
45. Rodríguez-Antuñano, I.; Barros, B.; Martínez-Sánchez, J.; Riveiro, B. Urban Infrastructure Vulnerability to Climate-Induced Risks: A Probabilistic Modeling Approach Using Remote Sensing as a Tool in Urban Planning. *Infrastructures* **2024**, *9*, 107. [CrossRef]
46. Namaiti, A.; Zeng, S. Framework for evaluating and optimizing of supply-demand matching between medical services and heat health risks: A case study of Zhongshan, China. *Sustain. Cities Soc.* **2025**, *131*, 106760. [CrossRef]
47. Zhang, C.; Yang, Y.; Yu, L. Assessing urban surface thermal environment and heat health risk in Chinese cities: A twenty-year study. *Urban Clim.* **2025**, *59*, 102304. [CrossRef]
48. Jiang, K.; Pan, Z.; Pan, F.; Wang, J.; Han, G.; Song, Y.; Zhang, Z.; Huang, N.; Ma, S.; Chen, X.; et al. The global spatiotemporal heterogeneity of land surface-air temperature difference and its influencing factors. *Sci. Total Environ.* **2022**, *838*, 156214. [CrossRef] [PubMed]
49. Naserikia, M.; Hart, M.A.; Nazarian, N.; Bechtel, B.; Lipson, M.; Nice, K.A. Land surface and air temperature dynamics: The role of urban form and seasonality. *Sci. Total Environ.* **2023**, *905*, 167306. [CrossRef] [PubMed]
50. Yu, Z.; Yao, Y.; Yang, G.; Wang, X.; Vejre, H. Spatiotemporal patterns and characteristics of remotely sensed region heat islands during the rapid urbanization (1995–2015) of Southern China. *Sci. Total Environ.* **2019**, *674*, 242–254. [CrossRef] [PubMed]
51. Yoo, C.; Im, J.; Weng, Q.; Cho, D.; Kang, E.; Shin, Y. Diurnal urban heat risk assessment using extreme air temperatures and real-time population data in Seoul. *Iscience* **2023**, *26*, 108123. [CrossRef] [PubMed]
52. Jing, C.; Zhou, W.; Lin, Y.; Li, C.; Liu, W.; Hua, Y.; Zhang, Z. Capacity of nighttime light data in measuring urban human activity: Evidence from SDGSAT−1 glimmer imagery and mobile phone data. *Int. J. Digit. Earth* **2025**, *18*, 2589016. [CrossRef]
53. Swanwick, R.H.; Read, Q.D.; Guinn, S.M.; Williamson, M.A.; Hondula, K.L.; Elmore, A.J. Dasymetric population mapping based on US census data and 30-m gridded estimates of impervious surface. *Sci. Data* **2022**, *9*, 523. [CrossRef] [PubMed]
54. Xu, M.; Cao, C.; Jia, P. Mapping Fine-Scale Urban Spatial Population Distribution Based on High-Resolution Stereo Pair Images, Points of Interest, and Land Cover Data. *Remote Sens.* **2020**, *12*, 608.
55. Bergeron, M.F.; DiLaura Devore, C.; Rice, S.G. Climatic Heat Stress and Exercising Children and Adolescents. *Pediatrics* **2011**, *128*, e741–e747. [CrossRef] [PubMed]
56. Fastl, C.; Arnberger, A.; Gallistl, V.; Stein, V.K.; Dorner, T.E. Heat vulnerability: Health impacts of heat on older people in urban and rural areas in Europe. *Wien. Klin. Wochenschr.* **2024**, *136*, 507–514. [CrossRef] [PubMed]
57. Meade, R.D.; Akerman, A.P.; Notley, S.R.; McGinn, R.; Poirier, P.; Gosselin, P.; Kenny, G.P. Physiological factors characterizing heat-vulnerable older adults: A narrative review. *Environ. Int.* **2020**, *144*, 105909. [CrossRef] [PubMed]
58. Wang, Z.; Liu, Y.; Wang, T.; Tang, S.; Wu, X. Supply and demand analysis of urban thermal environments regulation services from an accessibility perspective: A coupled thermal risk and green space cooling assessment model. *Urban Clim.* **2025**, *60*, 102356. [CrossRef]
59. Li, N.; Xu, J.; Li, X.; Qin, B.; Wang, Y.; Fu, D.; Zhong, K.; Qin, Z. A Novel Land Surface Temperature Retrieval Algorithm for SDGSAT-1 Images. *IEEE Trans. Geosci. Remote Sens.* **2025**, *63*, 5000218.
60. Liu, Y.; Yu, Y.; Yu, P.; Wang, H.; Rao, Y. Enterprise LST Algorithm Development and Its Evaluation with NOAA 20 Data. *Remote Sens.* **2019**, *11*, 2003. [CrossRef]
61. Rongali, G.; Keshari, A.K.; Gosain, A.K.; Khosa, R. Split-Window Algorithm for Retrieval of Land Surface Temperature Using Landsat 8 Thermal Infrared Data. *J. Geovis. Spat. Anal.* **2018**, *2*, 14. [CrossRef]
62. Jenks, G.F. The data model concept in statistical mapping. *Int. Yearb. Cartogr.* **1967**, *7*, 186–190.
63. Guo, H.; Dou, C.; Chen, H.; Liu, J.; Fu, B.; Li, X.; Zou, Z.; Liang, D. SDGSAT-1: The world's first scientific satellite for sustainable development goals. *Sci. Bull.* **2023**, *68*, 34–38.
64. Liu, C.; Ouyang, X.; Yang, J.; Gunasekera, D.; Weng, Q.; Zhao, X.; Sun, Z. Assessing the impact of urban block-scale landscape features on the diurnal cooling of green spaces using SDGSAT-1. *Ecol. Indic.* **2025**, *178*, 113937. [CrossRef]
65. Xie, Y.; Ma, C.; Zhao, Y.; Yan, D.; Cheng, B.; Hou, X.; Chen, H.; Fu, B.; Wan, G. The Potential of Using SDGSAT-1 TIS Data to Identify Industrial Heat Sources in the Beijing–Tianjin–Hebei Region. *Remote Sens.* **2024**, *16*, 768.
66. Gong, F.; Yang, Z.; Deng, S. Fine-scale assessment of diurnal heat health risk based on satellite and street view images. *Cities* **2025**, *162*, 105963. [CrossRef]

67. Wang, J.; Zhang, M. Diurnal-nocturnal heat health risk assessment at the block scale: Integrating urban functional zones and local climate zones. *Sustain. Cities Soc.* **2025**, *130*, 106609. [CrossRef]
68. Zeng, K.; Gao, F.; Peng, Y.; Liu, C.; Chen, W.; Li, G. Riding through the heat: Assessing heat health risk of cycling based on diurnal temperature and shared-bike big data. *Appl. Geogr.* **2025**, *184*, 103764. [CrossRef]
69. Wang, Y.; Huang, H.; Wu, B. Evaluating the Potential of SDGSAT-1 Glimmer Imagery for Urban Road Detection. *IEEE J. Sel. Top. Appl. Earth Obs. Remote Sens.* **2025**, *18*, 785–794.
70. Li, X.; Liu, Z.; Chen, X.; Meng, Q. Assessment of the impact of the 2010 Haiti earthquake on human activity based on DMSP/OLS time series nighttime light data. *J. Appl. Remote Sens.* **2019**, *13*, 044515. [CrossRef]
71. Antuñano, I.R. Repensar el urbanismo como solución al cambio climático. Caso de estudio: Área Metropolitana Asturiana. In *Proceedings of the IV ISUF-H International Conference: Cities and Forms: Urban Planning for the 21st Century: Urban and Metropolitan Forms*; DUOT, UPC: Barcelona, Spain, 2020; pp. 1–22.
72. Qureshi, A.M.; Rachid, A. Heat Vulnerability Index Mapping: A Case Study of a Medium-Sized City (Amiens). *Climate* **2022**, *10*, 113. [CrossRef]
73. Debone, D.; Rosário, N.M.É.D.; Miraglia, S.G.E.K. The Cost of Heat: Health and Economic Burdens in Three Brazilian Cities. *Atmosphere* **2025**, *16*, 755. [CrossRef]
74. Desai, V.K.; Wagle, S.; Rathi, S.K.; Patel, U.; Desai, H.S.; Khatri, K. Effect of ambient heat on all-cause mortality in the coastal city of Surat, India. *Curr. Sci.* **2015**, *109*, 1680–1686.
75. Kacker, K.; Srivastava, P.; Mukherjee, M. Heat stress risk at an intra-urban level: A case study of Delhi, India. *Build. Environ.* **2024**, *264*, 111897. [CrossRef]
76. Pierce, G.; Gabbe, C.J.; Dunlap, L.; Detwiler, B.; Garcia, P.U.; Hagen, H.; Schmidt, K. Planning for heat beyond the big city: Comparing smaller cities' heat activities, opportunities, and constraints in California. *Local Environ.* **2025**, *30*, 1403–1419. [CrossRef]
77. Amorim, M.C.D.C.; Dubreuil, V.; Teixeira, D.C.F.; Amorim, A.T.; Brabant, C. Exceptional heat island intensities also occur in medium-sized cities. *Urban Clim.* **2024**, *53*, 101821. [CrossRef]
78. Trego, S.; Meerow, S.; Keith, L. Heat planning in small and medium-sized cities: A collaborative application of PIRS™ for heat in Kent, WA, USA. *Socio-Ecol. Pract. Res.* **2023**, *5*, 409–422. [CrossRef]
79. Zezzo, L.V.; Coltri, P.P.; Dubreuil, V.; Torres, G.A.L.; de Costa Trindade Amorim, M.C. Exploring the urban heat island phenomenon in a tropical medium-sized city: Insights for sustainable urban development. *Environ. Monit. Assess.* **2025**, *197*, 445. [CrossRef] [PubMed]
80. Ngwenya, B.; Oosthuizen, J.; Cross, M.; Frimpong, K. Emerging heat-related climate change influences; a public health challenge to health care practitioners and policy makers: Insight from Bulawayo, Zimbabwe. *Int. J. Disaster Risk Reduct.* **2018**, *27*, 596–601. [CrossRef]
81. Adams, Q.H.; Chan, E.M.G.; Spangler, K.R.; Weinberger, K.R.; Lane, K.J.; Errett, N.A.; Hess, J.J.; Sun, Y.; Wellenius, G.A.; Nori-Sarma, A. Examining the Optimal Placement of Cooling Centers to Serve Populations at High Risk of Extreme Heat Exposure in 81 US Cities. *Public Health Rep.* **2023**, *138*, 955–962. [CrossRef] [PubMed]
82. Zou, Y.; Chen, J.; Yu, Y. Heat exposure risk assessment of street canyons around urban rail transit station areas: A case study of Shanghai. *Int. J. Disaster Risk Reduct.* **2025**, *123*, 105522. [CrossRef]
83. Zhu, W.; Yuan, C. Urban heat health risk assessment in Singapore to support resilient urban design—By integrating urban heat and the distribution of the elderly population. *Cities* **2023**, *132*, 104103. [CrossRef]
84. Kovats, R.S.; Hajat, S. Heat Stress and Public Health: A Critical Review. *Annu. Rev. Public Health* **2008**, *29*, 41–55. [CrossRef] [PubMed]
85. Antuñano, I.R. ¿Derecho a la ciudad? Una mirada a la distribución de los espacios verdes en Barcelona, desde la perspectiva de justicia ambiental. Master's Thesis, Universitat Politècnica de Catalunya, Barcelona, Spain, 2019.
86. Yi, S.; Li, X.; Ma, C.; Wang, R.; Zhou, Y.; Xu, Q.; Zhao, T. Assessing the differential impact of vegetated and built-up areas on heat exposure environment: A case study of Los Angeles. *Build. Environ.* **2025**, *271*, 112538. [CrossRef]

Disclaimer/Publisher's Note: The statements, opinions and data contained in all publications are solely those of the individual author(s) and contributor(s) and not of MDPI and/or the editor(s). MDPI and/or the editor(s) disclaim responsibility for any injury to people or property resulting from any ideas, methods, instructions or products referred to in the content.